AIAA−2002−0866
A NUMERICAL AND EXPERIMENTAL INVESTIGATION OF FLAPPING−WING PROPULSION IN GROUND EFFECT

K.D.Jones, B.M.Castro,
O.Mahmoud and M.F.Platzer

Naval Postgraduate School
Monterey, CA

40th Aerospace Sciences Meeting & Exhibit
14−17 January 2002 / Reno, NV

A NUMERICAL AND EXPERIMENTAL INVESTIGATION OF FLAPPING-WING PROPULSION IN GROUND EFFECT

K. D. Jones,[†] B. M. Castro, [‡] O. Mahmoud[⋆] and M. F. Platzer[⋆⋆]

Naval Postgraduate School
Monterey, California

Abstract

An experimental and numerical investigation of flapping-wing propulsion in ground effect is undertaken. Flying in ground effect is shown to have substantial performance advantages both in thrust and efficiency. To gain the performance advantage without requiring flight in the proximity of the ground, a bi-plane configuration is designed, providing increased performance as well as inherent balanced mechanical and aerodynamic loading. A high aspect-ratio experimental model is tested both qualitatively and quantitatively, using a smoke-wire for flow visualization, laser Doppler velocimetry for unsteady flow measurements, and a direct approach for thrust measurement. The configuration is simulated numerically using a two-dimensional, unsteady, inviscid panel code with a deforming wake model, and a two-dimensional, unsteady, compressible Navier-Stokes solver. The Navier-Stokes solver is used with a three-block, deforming grid, and it is run on a *Beowulf* Linux parallel cluster. Direct comparisons of thrust are made, as well as qualitative comparisons of the vortical wake structures produced by the wing-flapping. A strong Reynolds-number dependence is shown, reducing or eliminating the benefits of wake-interference at Reynolds numbers on the order of 10^4.

Nomenclature

a = speed of sound
A = aspect ratio, b/c
b = wing span
c = chord length
C_D = drag coefficient, drag/$(q_\infty S)$
$C_{D_{\text{stat}}}$ = drag coefficient of the non-moving wings
C_L = lift coefficient, lift/$(q_\infty S)$
C_P = power coefficient, power/$(q_\infty S U_\infty) = -C_L \dot{z}$
C_T = thrust coef., thrust/$(q_\infty S) = C_{D_{\text{stat}}} - C_D$
f = frequency in Hertz
h = plunge amplitude in terms of c
k = reduced frequency, $2\pi f c/U_\infty$
l = length scale used for Sr
M = Mach number
q = dynamic pressure, $\rho U^2/2$
Pr = Prandtl number
Re = chord Reynolds number, $U_\infty c/\nu_\infty$
S = wing area
Sr = Strouhal number, $lk/(2\pi)$
T = nondimensional time per period, $2\pi/k$
t = time
U_∞ = free-stream velocity
u, w = Cartesian velocity components
x, z = Cartesian coordinates in terms of c
$z(\tau)$ = vertical displacement in terms of c
η = propulsive efficiency, $\overline{C_T}/\overline{C_P}$
ν = kinematic viscosity
ϕ = phase angle through the flapping stroke
ρ = density
τ = nondimensional time, ta_∞/c
$\dot{(\ )}$ = rate of change with respect to τ
$\bar{(\ )}$ = averaged over one period
$|_{wall}$ = quantity on the surface of the airfoil
$(\ )_\infty$ = free-stream value

Introduction

The agile flight of birds and insects and the propulsion of aquatic animals have been sources of fascination for the curious throughout the ages. However, the lack of immediately apparent commercial or military applications has kept the funding level for scientific investigations devoted to these problems relatively low. It appears now that there is an increasing interest in the development of micro air and water vehicles which, in turn, raises the question of whether *unconventional* propulsion systems, such as those used by birds, insects and aquatic animals for millions of years, deserve a second look.

The first explanation of the bird's ability to generate a thrust force by means of flapping its wings seems to have been published by Knoller[1] in Vienna and Betz[2] in Göttingen in 1909 and 1912, respectively. Prandtl's student Birnbaum[3] first presented a solution for incompressible flow past flapping airfoils in 1924, while in 1922, Katzmayr,[4] in Vienna, pro-

[†] Research Assistant Professor, Senior Member, AIAA
[‡] Graduate Student, Student Member, AIAA
[⋆] Graduate Student, Student Member, AIAA
[⋆⋆] Professor, Fellow, AIAA

duced the first wind tunnel measurements which conclusively showed that an airfoil mounted in an oscillating wind stream experiences a thrust force. In 1936, Garrick[5] applied Theodorsen's theory to the problem of sinusoidally plunging and/or pitching airfoils and presented results valid for the whole reduced frequency range. In the 1940's and 50's Schmidt,[6] in East Germany, started to conduct systematic experiments on flapping foil propellers which led him to the development of the *wave propeller* and its demonstration on a catamaran boat.

Garrick showed that the propulsive efficiency of a single harmonically plunging airfoil was only about 50 percent unless the airfoil oscillated rather slowly (which in turn required a large airfoil in order to obtain significant thrust values). Schmidt sought to overcome this deficiency by arranging two airfoils in tandem, where the forward foil was oscillating and the rearward foil was stationary. This made it possible to convert the vortical energy generated by the forward foil into additional thrust rather than being wasted. Schmidt claimed that his wave propeller achieved efficiencies comparable to those of conventional propellers and had the additional advantage of enabling operation in shallow waters. The only predictive tool available to Schmidt was Theodorsen's inviscid oscillatory thin airfoil theory - a tool of only marginal utility. Therefore, he arrived at his wave propeller by pure experimentation.

More recently, Jones and Platzer[7,8] looked at Schmidt's wave propeller as well as another *wake interference* configuration, as shown in Fig. 1. Case (a) is the single flapping wing, case (b) is a model of the Schmidt *wave-propeller*, with a flapping fore-wing and stationary trailing-wing, and case (c) is the biplane configuration, which emulates a wing flapping in ground effect. An unsteady panel code was used to evaluate these three cases, and the results clearly demonstrated the benefits of exploiting wake interference to improve performance. The time-averaged thrust coefficient and propulsive efficiencies predicted by Garrick's linear theory and the panel code are plotted in Figs. 2 and 3, respectively. The values plotted for cases (b) and (c) are average values for the two wings. The forward airfoil produces almost all of the thrust in case (b), but both airfoils perform equally in case (c). Birds that fly low over water seem to have discovered the advantages of configuration (c).

Garrick's theory was only applicable for the single-wing case, and the agreement with the panel code was quite good at low frequencies, degrading at higher frequencies. It was shown that the primary deficiency of Garrick's theory is the inability to model out-of-plane vorticity.

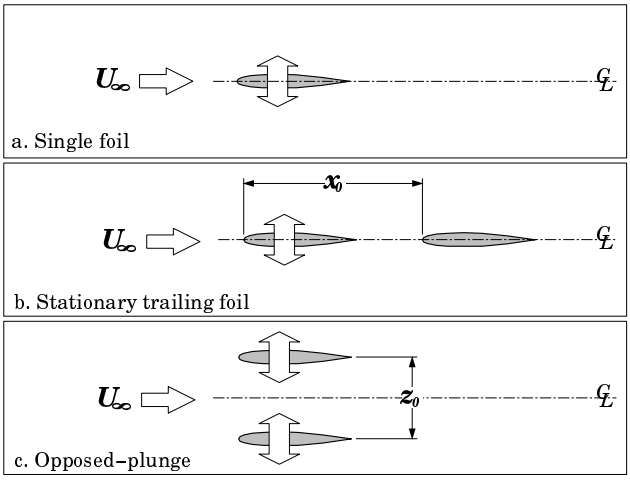

Fig. 1: Numerical and experimental configurations investigated.

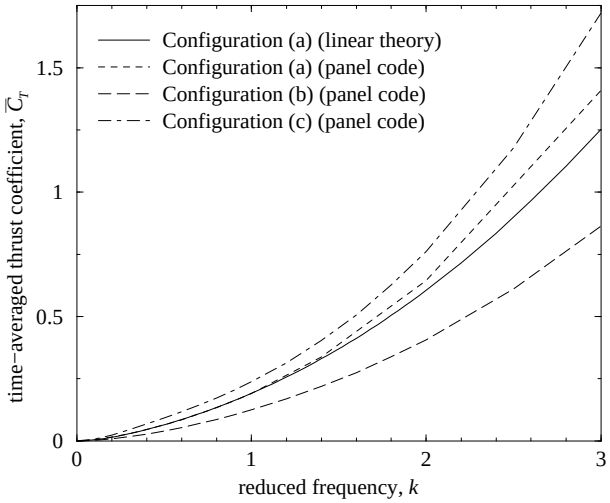

Fig. 2: Thrust coefficient versus reduced frequency.

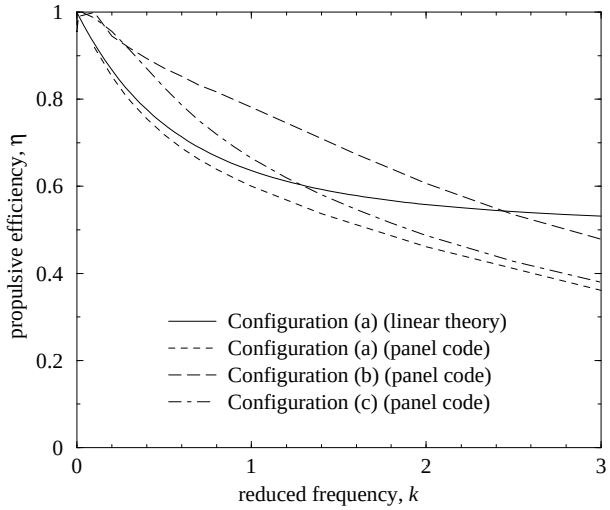

Fig. 3: Efficiency versus reduced frequency.

While case (b), the *wave-propeller*, was found to produce the highest efficiency over the full frequency range, it was noted that due to the much lower average thrust coefficient, viscous losses, which are not considered in the panel-code solutions would greatly reduce overall performance, particularly at lower Reynolds numbers. On the other hand, case (c), the bi-plane or ground-effect case, produced roughly double the thrust of (b), and still at a higher efficiency than (a). Case (c) offered the additional benefit of being mechanically and aerodynamically balanced.

A mechanical model of case (c) was designed, manufactured and tested in Jones and Platzer.[8] The model, pictured in Fig. 4, flapped two, high aspect-ratio wings sinusoidally, with a maximum amplitude of $h = 0.4$. The wings had an airfoil section resembling a NACA 0014, with a 64 mm chord, and an overall span of 1200 mm. Flapping frequencies up to about 8 Hz were possible.

To measure thrust, the model was suspended from the tunnel ceiling on four thin cables, as shown in Fig. 5, such that it could swing freely in the flow-direction but remained stable in all other directions. If thrust or drag was produced, the model was displaced in the streamwise direction, and the displacement was measured using a laser range-finder placed downstream of the model. By calibrating against known forces, the thrust could be determined.

Experiments were performed in the Naval Postgraduate School low-speed wind-tunnel, shown in Fig. 6, a continuous, flow-through facility with an approximate flow-speed range between 0 and 10 m/s. The measured thrust for a range of flow speeds and flapping frequencies is shown in Fig. 7, with the velocities corrected by Lund.[9] The agreement with the panel code was quite reasonable, especially considering that the experimental Reynolds numbers were between about 1.0×10^4 and 4.5×10^4. In particular, the trend toward increasing thrust with increasing flow-speed was encouraging. It was noted that at lower flow speeds and higher flapping frequencies (meaning high k), the measured performance dropped off sharply into something resembling a drag bucket. The induced angle of attack in this region exceeded 14 degrees, and it was thought that flow separation may be the cause of the degradation in performance.

In the following years the bi-plane configuration evolved into a flapping-wing design for Micro Air Vehicles (MAVs), such as the model shown in Fig. 8.[10,11] The MAVs were designed around the DARPA criteria limiting them to a 15 cm length and span. The models had weights between about 6 and 10 grams, and the tiny stepping motors could drive them up to flapping frequencies of about 40 Hz.

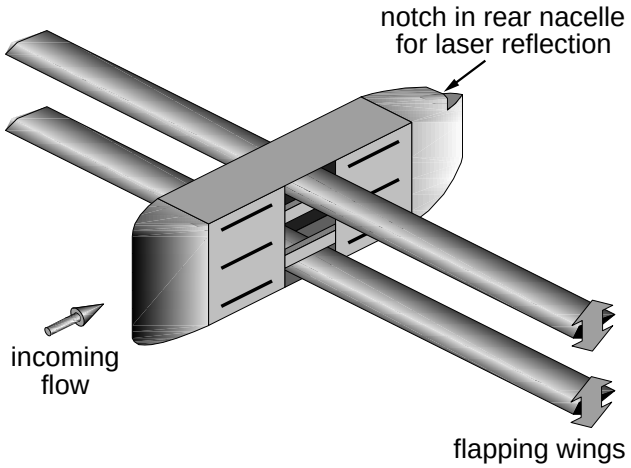

Fig. 4: Isometric view of the large model.

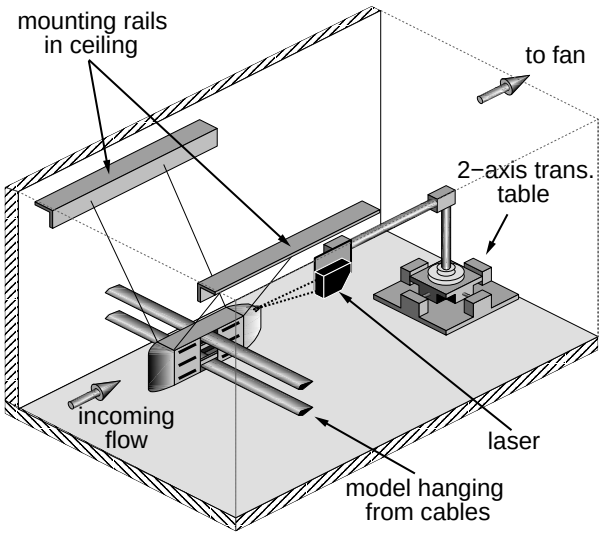

Fig. 5: View of the large model in the test-section.

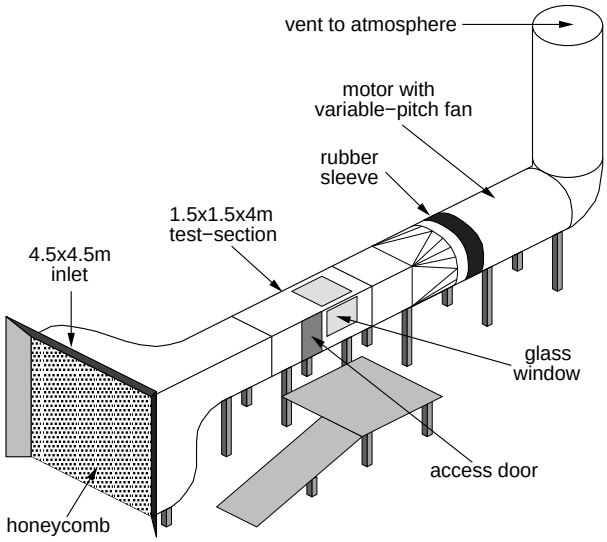

Fig. 6: Schematic of the NPS low-speed wind tunnel.

Thrust for the MAVs was measured in a similar way to the larger model, but the support cables were replaced with 0.13 mm diameter, single-strand, bare copper wire. As well as supporting the model, the copper wires also provided a means to feed power to the motor, with 3 of the wires going to the 3 poles on the stepping motor, and the 4th providing a back-EMF signal for the closed-loop motor controller.

Typical performance of a MAV is shown in Fig. 9, and contrary to what was found for the large flapping model, the MAV performance decreased rapidly with velocity. This was partially due to a passive feathering mechanism, but it was also thought that flow separation played an important role in this behavior. Flow visualization verified that flow separation existed, but the reason for the high performance at zero or very low speeds, and low performance at higher speeds was unknown.

It became clear that the panel code could not accurately model the flow physics for the MAVs. Therefore, for the present investigation, a two-dimensional, unsteady, compressible Navier-Stokes solver was used to duplicate the experiment, providing a means to predict separation-induced losses in the performance, and for the first time, a means of evaluating the Reynolds number dependence of the flows.

In the following sections, details of the numerical methods are presented, a few additional details of the experimental methods are given, and results from the two are compared both qualitatively and quantitatively.

Configuration

The geometry and motion of the bi-plane configuration are shown in Fig. 10. The dimensions and motion duplicate the limits of the large flapping model. The wings undergo a pure cosine plunge motion at zero angle of attack. The plunge amplitude is $0.4c$, and the mean separation between the two wings is $1.4c$, which mimics a single wing flapping at $0.7c$ above the ground. Note, the two wings must flap in counter-phase in order to enforce the symmetry condition.

Numerical Approach

Both an unsteady panel method and an unsteady Navier-Stokes solver are used in the present study. The panel code has been used in many similar studies, and is only briefly described here for clarity. A number of modifications were made to the Navier-Stokes code to enable these simulations, including domain-decomposition, deforming grids, and parallel computation, and these modifications are described in greater detail.

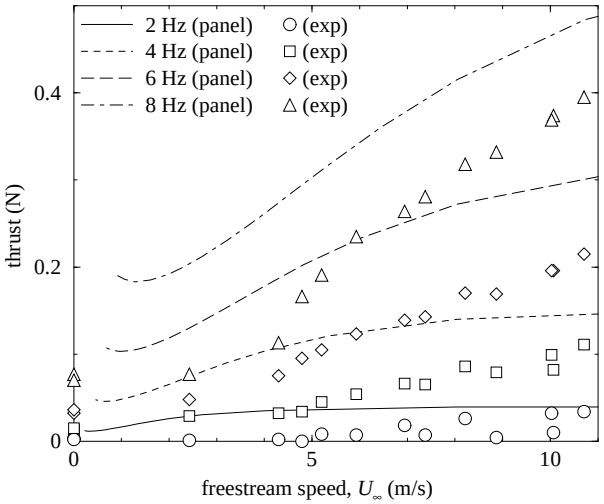

Fig. 7: Measured and predicted thrust for the large model.

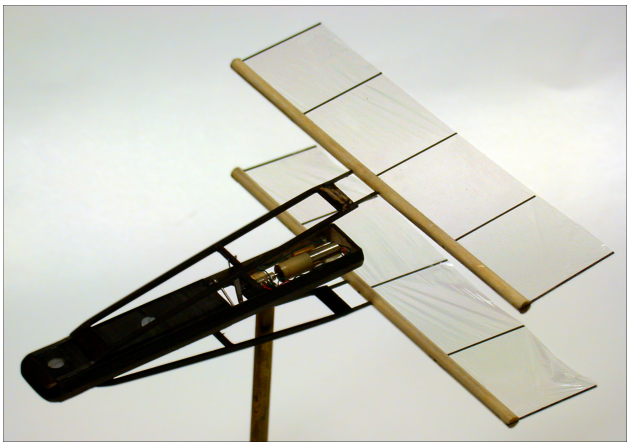

Fig. 8: Typical 15 cm length/span MAV model.

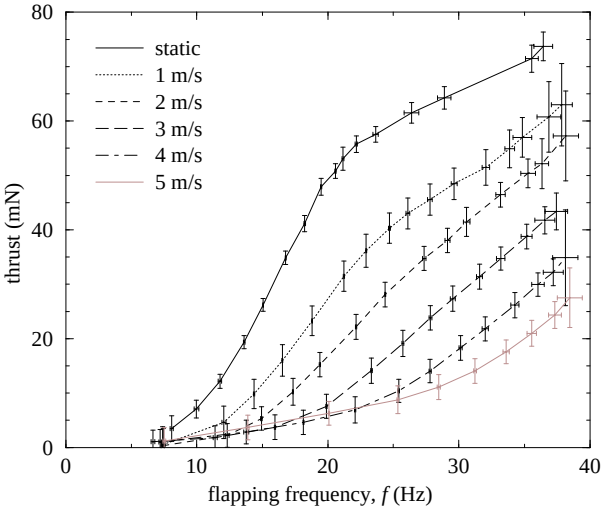

Fig. 9: Measured thrust for a typical MAV model.

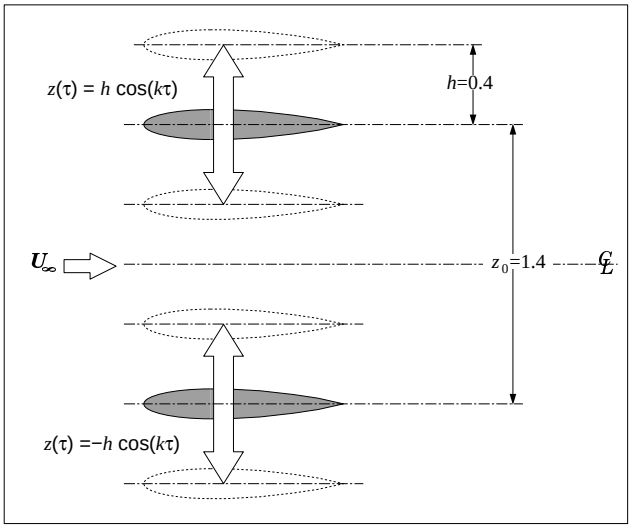

Fig. 10: Geometry of the bi-plane model.

Panel Code

Panel code solutions were performed with an unsteady, potential-flow code, originally developed by Teng[12] with additional features and a Graphical User Interface (GUI) developed by Jones and Center.[13] The basic approach follows the method of Hess and Smith,[14] with the vorticity shedding procedure of Basu and Hancock[15] for unsteady simulations. The code was extended to the modeling of two-airfoil systems by Platzer *et al.*[16]

The method includes a deforming wake model, where a discrete vortex is shed from each airfoil trailing edge at the end of each time step to offset the change in circulation about the airfoil. These vortices convect downstream, influencing each other and the airfoils, providing a surprisingly accurate model of the unsteady wake roll-up, such as that shown in Fig. 11, for a simulation of the large model, flapping at $k = 1.5$, where the discrete wake vortices are represented by the small squares.

Details of the panel code and its validation can be found in the cited references, as well as in Refs. 7, 8, 17 and 18.

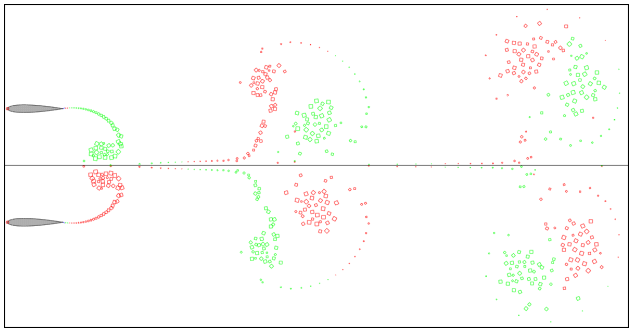

Fig. 11: Symmetric panel-code wake model for k=1.5.

Navier-Stokes Code

The numerical methods utilized for the Navier-Stokes simulations are summarized in some detail in the following sections, with more detailed information available in Castro.[19]

Governing Equations The time-dependent, compressible, two-dimensional, thin-layer Navier-Stokes equations in the strong conservation law form and curvilinear coordinate system (ξ, ζ) are:

$$\partial_t \hat{\mathbf{Q}} + \partial_\xi \hat{\mathbf{F}} + \partial_\zeta \hat{\mathbf{G}} = Re^{-1} \partial_\zeta \hat{\mathbf{S}} \tag{1}$$

where $\hat{\mathbf{Q}}$ is the vector of conservative variables,

$$\hat{\mathbf{Q}} = \frac{1}{J} \begin{Bmatrix} \rho \\ \rho u \\ \rho w \\ e \end{Bmatrix}, \tag{2}$$

$\hat{\mathbf{F}}$ and $\hat{\mathbf{G}}$ are the inviscid flux vectors,

$$\hat{\mathbf{F}} = \frac{1}{J} \begin{Bmatrix} \rho U \\ \rho u U + \xi_x p \\ \rho w U + \xi_z p \\ (e+p)U - \xi_t p \end{Bmatrix}, \tag{3}$$

$$\hat{\mathbf{G}} = \frac{1}{J} \begin{Bmatrix} \rho W \\ \rho u W + \zeta_x p \\ \rho w W + \zeta_z p \\ (e+p)W - \zeta_t p \end{Bmatrix}, \tag{4}$$

and $\hat{\mathbf{S}}$ is the thin-layer approximation of the viscous fluxes in the ζ direction (normal to the airfoil surface),

$$\hat{\mathbf{S}} = \frac{1}{J} \begin{Bmatrix} 0 \\ \mu m_1 u_\zeta + (\mu/3) m_2 \zeta_x \\ \mu m_1 w_\zeta + (\mu/3) m_2 \zeta_z \\ \mu m_1 m_3 + (\mu/3) m_2 m_4 \end{Bmatrix}, \tag{5}$$

where

$$m_1 = \zeta_x^2 + \zeta_z^2, \tag{6}$$
$$m_2 = \zeta_x u_\zeta + \zeta_z w_\zeta, \tag{7}$$
$$m_3 = \partial_\zeta (u^2 + w^2)/2 + (\gamma - 1)^{-1} Pr^{-1} \partial_\zeta (a^2), \tag{8}$$
$$m_4 = \zeta_x u + \zeta_z w. \tag{9}$$

The terms U and W are the contravariant velocity components given by:

$$U = u\xi_x + w\xi_z + \xi_t \tag{10}$$
$$W = u\zeta_x + w\zeta_z + \zeta_t \tag{11}$$

and J is the metric Jacobian, where

$$J^{-1} = x_\xi z_\zeta - x_\zeta z_\xi \ . \tag{12}$$

The pressure is related to the other variables through the equation of state for an ideal gas

$$p = (\gamma - 1)\Big[e - \rho(u^2 + w^2)/2\Big] \ . \qquad (13)$$

Eqs. (1-13) are nondimensionalized using c as the reference length, a_∞ as the reference speed, c/a_∞ as the reference time, ρ_∞ as the reference density and $\rho_\infty a_\infty^2$ as the reference energy.

Numerical Methods The numerical solution algorithm was developed and tested by Ekaterinaris and Menter.[20] Oscillatory motion of the airfoil in the proximity of the ground plane (symmetry plane) required the use of deforming grids, and therefore, the method suggested by Thomas and Lombard[21] was used to account for temporal grid deformation, better known as the Geometric Conservation Law (GCL). The algorithm is given by:

$$\begin{aligned}
&\Big[I + h_\xi\Big(\nabla_\xi \hat{A}^+_{i,k} + \Delta_\xi \hat{A}^-_{i,k}\Big)\Big]^p \\
&\times\Big[I + h_\zeta\Big(\nabla_\zeta \hat{B}^+_{i,k} + \Delta_\zeta \hat{B}^-_{i,k} - Re^{-1}\delta_\zeta \hat{M}_{i,k}\Big)\Big]^p \\
&\times\Big(\hat{Q}^{p+1}_{i,k} - \hat{Q}^p_{i,k}\Big) \\
= \ &-\Big[\Big(\hat{Q}^p_{i,k} - \hat{Q}^n_{i,k}\Big) \\
&+ h_\xi\Big(\hat{F}^p_{i+1/2,k} - \hat{F}^p_{i-1/2,k}\Big) \\
&+ h_\zeta\Big(\hat{G}^p_{i,k+1/2} - \hat{G}^p_{i,k-1/2}\Big) \\
&- Re^{-1}h_\zeta\Big(\hat{S}^p_{i,k+1/2} - \hat{S}^p_{i,k-1/2}\Big)\Big] \ . \qquad (14)
\end{aligned}$$

In Eq. (14), $h_\xi = \Delta\tau/\Delta\xi$ etc., $\hat{A}^\pm = \partial\hat{F}/\partial\hat{Q}$ etc. are the flux Jacobian matrices and ∇, Δ and δ are the forward, backward and central difference operators, respectively. The quantities $\hat{F}_{i+1/2,k}$, $\hat{G}_{i,k+1/2}$ and $\hat{S}_{i,k+1/2}$ are numerical fluxes. The superscript $(\cdot)^n$ denotes the physical time step, and the superscript $(\cdot)^p$ refers to Newton sub-iterations within each physical time step. The Jacobian of the transformation of the deformed grid at the $n+1$ time step is J^{n+1}, and $\Delta J = -\Delta\tau[\xi_t^{n+1} + \zeta_t^{n+1}]$.

The inviscid fluxes, $\hat{F}$ and $\hat{G}$, are evaluated by means of Osher's third-order accurate, upwind-biased scheme.[22,23] Linearization of the left-hand side of Eq. (14) is performed by evaluating the flux Jacobian matrices, A and B, with the Steger-Warming flux-vector splitting.[24] The viscous fluxes are computed with second-order central differences. Furthermore, a standard min-mod TVD flux limiter[23] is used to eliminate numerical oscillations at shocks developed at transonic Mach numbers. However, Mach numbers in this investigation remained subsonic.

Time accuracy is improved by performing Newton sub-iterations to convergence within each physical step. These sub-iterations minimize the linearization and factorization errors and help drive the left-hand side of Eq. (14) to zero. Numerical experiments have shown that larger CFL numbers (i.e., a larger time step) could be used if the number of Newton iterations was increased.

The turbulence modeling is based either on the standard algebraic model of Baldwin and Lomax[25] or one equation models of Baldwin and Barth[26] or Spalart and Allmaras.[27] The eddy-viscosity obtained from the models is used for the computation of the fully turbulent region.

Computational Grids The bi-plane configuration introduces several gridding difficulties stemming from the need to model two surfaces with an unsteady relative motion. To minimize the computational effort, a symmetry condition is applied at the ground plane, contrary to the panel code, where a second airfoil is included and the symmetry is implied.

A deforming mesh is used to handle the flapping motion of the wing, and due to the close proximity of the wing to the ground plane, a multi-block grid is needed, as illustrated in Fig. 12, where block 1, surrounding the airfoil, is deforming, block 2 is a Cartesian grid upstream of block 1, and block 3 is a Cartesian farfield grid. Using a single deforming mesh would require severely skewed grid cells over much of the computational space, but in the three-block arrangement, the block containing the wing is a compact, well-ordered C-grid, and the other two blocks are relatively sparse rectangular grids.

Only block 1 deforms, and it is divided up into several regions, as shown in Fig. 13. Region A, surrounding the airfoil, is moved as a rigid body, ensuring a uniform grid quality in the boundary layer. Region C, the outer boundary, is also rigid in order to simplify data transfer to the other blocks. Region D, surrounding the wake cut line, follows the airfoil motion at the upstream end, and remains fixed at the downstream end, and smoothly deforms in between. Lastly, region B deforms to account for the relative motion of the other areas.

The grid is generated using a simple algebraic routine, and must be regenerated at every time step. Detailed views of the undistorted and maximally distorted grids are shown in Figs. 14 and 15, respectively. Portions of blocks 2 and 3 are shown as the lighter colored regions.

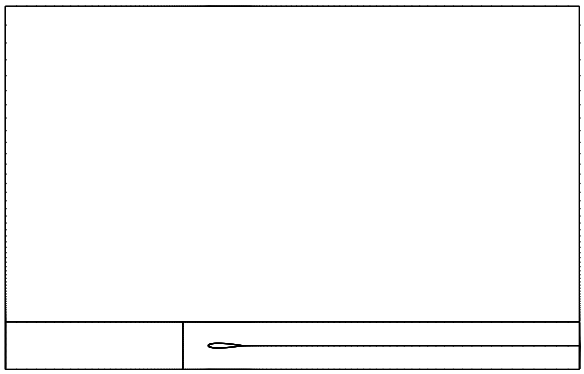

Fig. 12: Outline of the 3-block grid.

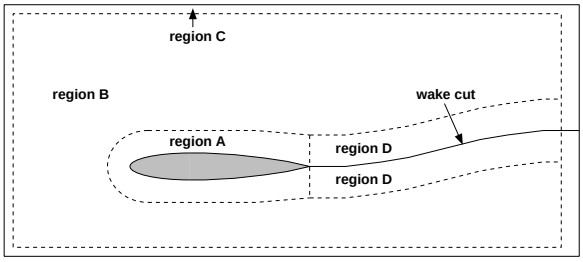

Fig. 13: Rigid and deforming grid regions of block 1.

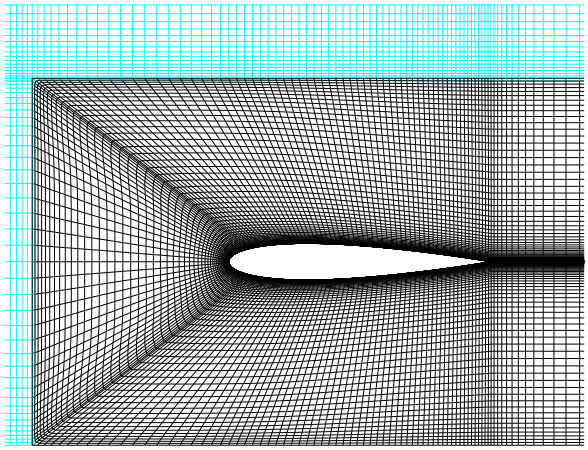

Fig. 14: Grid detail near the airfoil.

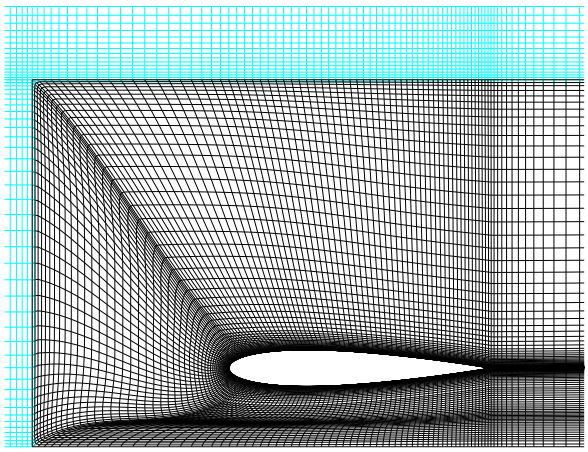

Fig. 15: Distorted grid detail near the airfoil.

The Navier-Stokes grid system used in the study had 281×81 points in block 1, 41×31 points in block 2, and 165×51 points in block3. Grid refinement studies as well as single versus multi-block grid comparisons were performed, and are detailed by Castro.[19] The wall spacing was set to yield $y^+ < 1$ for a Reynolds number of 10^6, and is actually much finer than necessary for the lower Reynolds number simulations.

Boundary Conditions For inviscid flow solutions, the viscous terms on the RHS of Eq. (1) are set to zero, and flow-tangency boundary conditions are used at the surface. For Navier-Stokes solutions, the no-slip condition is applied. Density and pressure are extrapolated to the wall for both Euler and Navier-Stokes solutions.

For unsteady airfoil motions, the flow-tangency and no-slip conditions are modified to include the local motion of the surface which also contributes to the pressure on the surface. Therefore, the momentum equation normal to the surface (ζ direction) is solved to predict the pressure for a viscous flow more accurately

$$\partial_\zeta p|_{wall} = -\frac{1}{\nabla^2 \zeta}\left[\rho\, \partial_t \begin{Bmatrix} \dot{x}|_{wall} \\ \dot{z}|_{wall} \end{Bmatrix} \cdot \nabla\zeta + \partial_\zeta \rho|_{wall} \nabla\xi \cdot \nabla\zeta\right], \qquad (15)$$

where $\dot{x}|_{wall}$ and $\dot{z}|_{wall}$ are the Cartesian components of the airfoil velocity. Furthermore, by assuming that the grid is orthogonal at the surface $\nabla\xi \cdot \nabla\zeta = 0$. If the airfoil is stationary, the normal pressure gradient vanishes in agreement with boundary-layer theory.

Inflow and outflow boundary conditions are imposed on the outer boundary faces, and a symmetry condition is applied at the lower boundary of blocks 1 and 2. For the inflow boundary, flow properties such as pressure, temperature, and velocity are specified while the density is extrapolated from the neighboring interior points. Static pressure is specified for the outflow boundary condition and all other properties are extrapolated from the interior. Boundary conditions on the interior boundaries are handled using interpolated data from a row of overlapping grid points in the adjacent grid. The symmetry boundary condition is enforced by setting the normal velocity to zero and setting the gradient of all other flow variables to zero.

Experimental Approach

The experimental model was described in some detail in the introduction, with additional information and detailed images of the mechanism available in the cited references. The rest of the experimental apparatus is outlined in this section.

Flow speed in the wind tunnel (shown in Fig. 6) is measured either with a pitot-static tube, mounted about 0.5 m above the model, and a MKS Baratron type 223B differential pressure transducer or using Laser Doppler Velocimetry (LDV). The LDV system uses a 5W, water-cooled Coherent Innova Argon-ion laser coupled with a three-component TSI system to separate, split and shift the beams, a two component fiber optic probe with 50 mm beam separation and a 750mm lens, a TSI 755 signal processor (currently with just one channel), and a PC fitted with a DMA card and the TSI FIND and PACE software. For unsteady measurements a Rotary Motion Resolver (RMR) was added to the system. Flow seeding was performed using a TSI six jet atomizer, using compressed air and distilled water, yielding roughly 1 micron sized particles. Details of the LDV techniques and equipment can be found in Mahmoud.[28]

For thrust measurements, the model is suspended in the pendulum arrangement shown in Fig. 5, with LDV used to measure the freestream speed. As mentioned earlier, the thrust is determined by measuring the streamwise displacement of the model by bouncing a laser range finder off of a notch in the rear nacelle.

Flow visualization is performed using a smoke wire, constructed out of 0.25 mm diameter Ni80/Cr20 wire, wrapped with bands of 0.13 mm copper wire at 10 mm intervals along the wire. Roscoe fog juice is dripped down the wire using a pressurized system, and the wire is heated by running a current through it. As it heats, the fog fluid burns and releases smoke. The fluid pools on the copper bands so that discrete streaklines are released for 15 to 20 seconds. The smoke wire is only useful between about 1 and 3 m/s. at slower speeds the smoke is too hot and rises, providing an apparent angle of attack. At higher speeds the wire begins to shed a vortex street, and the streaklines rapidly dissipate. Visualization works well for chord-Reynolds numbers between about 0.5×10^4 to 1.5×10^4.

For the analysis of unsteady phenomena, several methods were used to record the visualization results. An adjustable strobe light was used to measure the frequency of flow features, such as the shedding of a vortex street, where the strobe's frequency was adjusted until the streaklines appeared frozen. Unfortunately, while the strobe is sufficiently bright for the naked eye, it was not bright enough for digital photography. To photograph the visualization, the streaklines were flooded with high-power halogen cinema lights, and a digital video camera was used to record the data. While the video camera would only shoot 30 frames per second, it would allow for very fast shutter, speeds, and at speeds of about 1/500th to 1/1000th of a second, the streaklines were quite clear.

Results

As previously mentioned, the primary deficiency with the use of the panel code for these simulations was the inability to predict flow separation and related losses. The prediction of these viscous phenomena are further complicated by the low Reynolds numbers of the experiment; typically less than 4×10^4. While past studies have provided significant experience with the unsteady solver, it had never been applied to these low Reynolds numbers. Clearly, the available turbulence and transition models, all developed for high Reynolds numbers, were of no use. Consequently, for simulations run at a Reynolds number of 10^4, fully laminar flow was assumed. Additionally, the code is compressible, and while the actual wind tunnel Mach numbers were less than 0.03, the code does not run well for Mach numbers below 0.1. Note, while for steady flows, compressible effects are generally neglected for Mach numbers up to about 0.3, for these flapping-wing simulations, at a reduced frequency of 2, simulations with a freestream Mach number of 0.3 will go transonic.

Several test simulations were performed to gain confidence in the use of the solver at low Reynolds and Mach numbers. The simplest comparison is for a single fixed wing at zero angle of attack. At high Reynolds numbers, steady flow is predicted. However, at a Reynolds number of 10^4, a vortex street is found in the wake, as shown in Fig. 16. In Fig. 17 the computed streaklines are shown for the same case. Using a strobe light, the reduced frequency of the street was measured at $k \approx 14.5$, whereas the Navier-Stokes solver predicted $k \approx 12.3$.

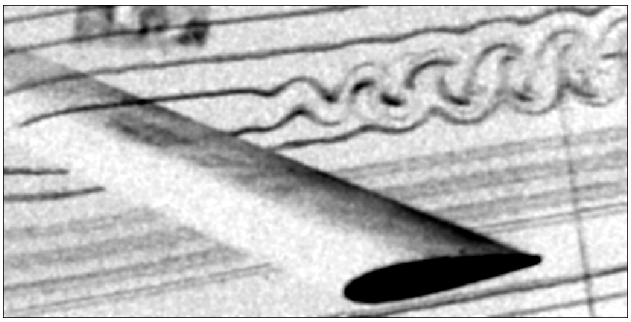

Fig. 16: Experimental streaklines for Re=10,000.

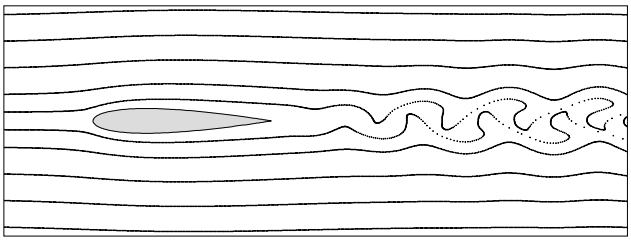

Fig. 17: Numerical streaklines for Re=10,000.

Using the airfoil thickness as the length scale, the Strouhal numbers of the wakes are 0.33 and 0.27, respectively; somewhat higher than the Strouhal number for the Kármán vortex street behind a cylinder (0.21).

While the numerically predicted shedding frequency was about 15 percent low, it was noted that the predicted shedding frequency increased as smaller time-steps and/or more Newton sub-iterations were used. This is shown in Fig. 18, where the time-history of the lift and drag coefficients predicted by the Navier-Stokes code are plotted for laminar flow at $Re = 10^4$. After the initial transients faded, the lift appeared to converge to a steady value for quite some time, and then oscillations began. A relatively large time step was used until about $\tau = 30$, and then the time-step was halved, resulting in a reduction in the amplitude of the lift oscillations, a reduction in drag and an increase in the shedding frequency. The time-step was reduced again at about $\tau = 35$, with 7,200 steps/cycle during the last 6 cycles. A total of about 200,000 time-steps with 8 Newton sub-iterations/step were required for this simulation.

The sensitivity to time-step was probably heightened by the very tight spacing of the grid at the airfoil surface and along the wake cut-line. The grid was structured for y^+ values of about 1 at $Re = 10^6$, but the y^+ values $Re = 10^4$ were less than 0.25, which may have contributed to this dependence. In the future, grids more appropriate for the low Reynolds numbers will be tested.

For the low-Re, laminar flow simulations, when the airfoils are flapped, the shedding persists, resulting in several superimposed frequencies in the resultant forces, as shown in Fig. 19, where the unsteady lift and drag predicted by the panel code and the Navier-Stokes solver are compared for $k = 1$. The panel code and the high Reynolds number Navier-Stokes results agree well, with minor differences due to compressibility and viscosity. Both the panel code and the high-Re results predict a negative drag throughout most of the flapping cycle, but the low-Re results predict a significant increase in overall drag and a reduction in the thrust peaks. Additionally, a high-frequency oscillation is apparent in the lift for the low-Re case. While bi-plane simulations have not been run at reduced frequencies below 0.5, single-airfoil simulations at reduced frequencies below about 0.4 result in solutions that are not periodic, but rather, they fit an *attractor*. However, at higher reduced frequencies, both the single-airfoil and bi-plane solutions yield essentially periodic solutions, even though the higher shedding frequencies are still present. This is shown in Fig. 20 where the lift is plotted as a function of $z(\tau)$ for $k = 1$.

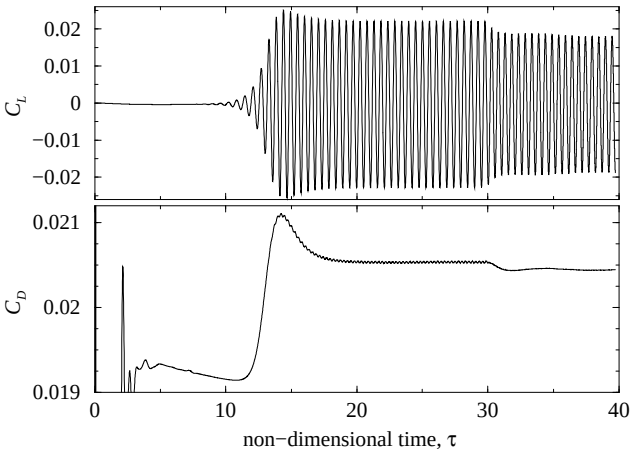

Fig. 18: Time-history of lift and drag for the stationary airfoil.

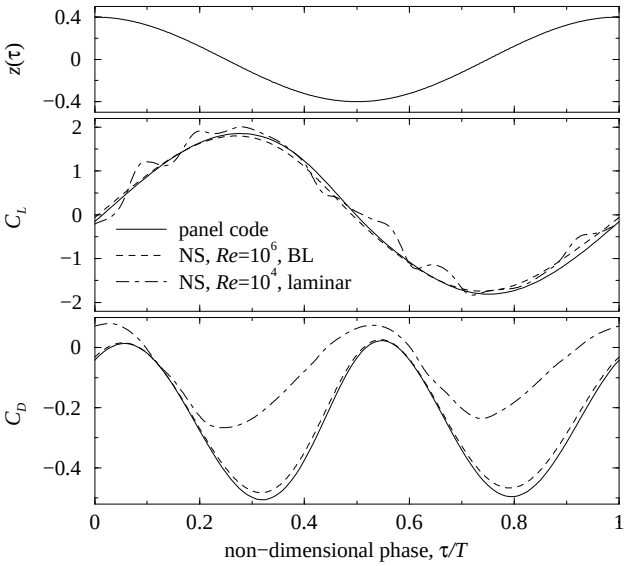

Fig. 19: Time-history of lift and drag for k=1.

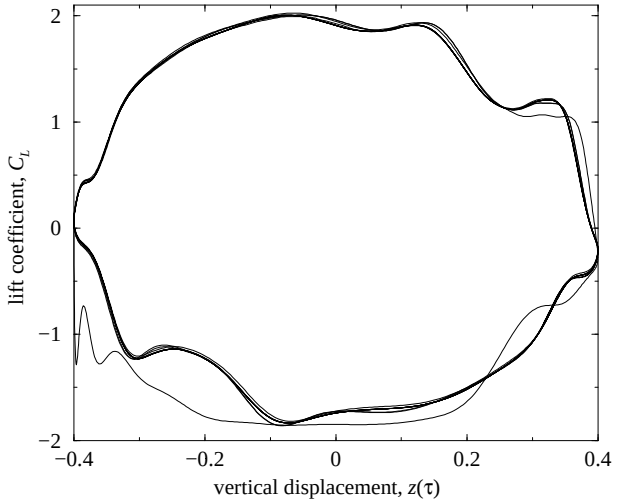

Fig. 20: Lift versus vertical displacement for k=1.

While the stationary airfoil sheds a vortex street at low-Re, the flapping airfoil produces a series of dynamic stall vortices for reduced flapping frequencies above about 0.2. Separation appears to initiate at the trailing edge, progressing toward the leading edge as the flapping frequency (and hence the induced angle of attack) is increased. These dynamic stall vortices have a dramatic effect on the wake, as shown in Fig. 21, where experimental and numerical streaklines are shown.

For the experimental photographs, a smoke wire was placed about 5 chordlengths upstream of the leading edge, with streaklines spaced at roughly 1 cm intervals. The wings were flapped at about 5.6 Hz with a freestream speed of about 2.25 m/s, resulting in $Re = 10^4$ and $k = 1$. The wake was flooded with high-power lights, and a digital video camera, running at 30 frames per second, and a shutter speed of 1/500th second, was used to record the streaklines. This resulted in about 5.4 frames per cycle, and 6 consecutive frames are shown on the left side of Fig. 21, covering almost a complete cycle. While the precise phase angles of the photos are not known, approximate values are included in the lower, left corners of the photos.

The numerically predicted streaklines for similar phase angles are shown on the right, where the numerical streaklines are produced by releasing discrete particles into the flow at regular intervals, and tracking them as they convect through the unsteady flowfield. Presently the particles are only tracked in grid block 1, and therefore, particles that leave the block are lost, resulting in breaks in the streaklines. Also, due to the restriction to block-1, the particles are released just 0.25 chordlengths upstream of the leading edge, greatly diminishing the up-stream influence on the particle paths. Despite these differences, the comparison is quite good.

The Reynolds-number dependence of the lift and drag, previously shown in Fig. 19, can also be seen in the predicted streaklines, as shown in Fig. 22. For these conditions ($k = 1$, $h = 0.4$), the induced angle of attack reaches about 21 degrees. In the high-Re solution, flow-separation is rather subtle, without noticeable dynamic stall vortices. However, at low-Re, a series of dynamic stall vortices is shed which greatly alter the structure of the wake. The excellent agreement between the lift and drag predicted by the panel code and the high-Re Navier-Stokes solution, shown in Fig. 19, is further supported by the wake topologies predicted by the two, shown in the center and lower portions of Fig. 22.

In Fig. 23, the time-averaged u-velocity in the wake is shown, for a cross-section one chordlength downstream of the trailing edge. The experimental data, measured using LDV, have been corrected for a slight velocity gradient across the test section (approximately 1 percent per chordlength in z in the tested region). The agreement with the low-Re solution is quite good. Note, the mean positions of the airfoils are at $z = \pm 0.7$ with $h = 0.4$. The trend toward narrower jet-like regions with decreasing Reynolds number is consistent with the single-airfoil solutions. The experimental velocity error bars illustrate the standard deviation of the freestream speed. The deviation of the unsteady flow was not measured.

In Fig. 24 the predicted and measured thrust coefficients are plotted as functions of the reduced frequency. Note, as indicated in the nomenclature, the thrust coefficient has the static drag removed in all cases. In the experiment, the same reduced frequency can be obtained for an infinite variation of flapping frequencies and flow speeds, which provides some measure of the Reynolds number dependence of the data. Consequently the experimental results have been divided into several groups, based on Reynolds number. The experimental results are bracketed pretty well between the high and low-Re Navier-Stokes results, with a clear trend as the Reynolds number decreased. The panel code and the high-Re results agree very well until $k > 1.5$, where separation becomes significant. Note, this is the only case where the difference between the BL and SA turbulence models was noticeable, with the BL model predicting a greater separation.

In Figs. 25 and 26 the predicted thrust coefficients and propulsive efficiencies for the single-airfoil and the bi-plane configuration are compared. For the high-Re case, only the BL turbulence model is shown. In all cases, the high-Re results agree well with the panel code except for the highest reduced frequency, with the bi-plane configuration yielding higher performance than the single wing. However, for the low-Re case, the two configurations perform about the same, with only minor advantages at lower reduced frequencies. This might explain why larger birds, like seagulls and pelicans, often fly low enough over water to benefit from the ground plane, but small birds and insects generally do not fly close enough to the surface to be affected.

Conclusions

In several previous investigations, the performance advantages of a wing flapping in ground effect were established, and a bi-plane configuration was devised to take advantage of the favorable wake-interference while providing an aerodynamically and mechanically balanced system. However, experimental results suggested a rather severe Reynolds number dependency.

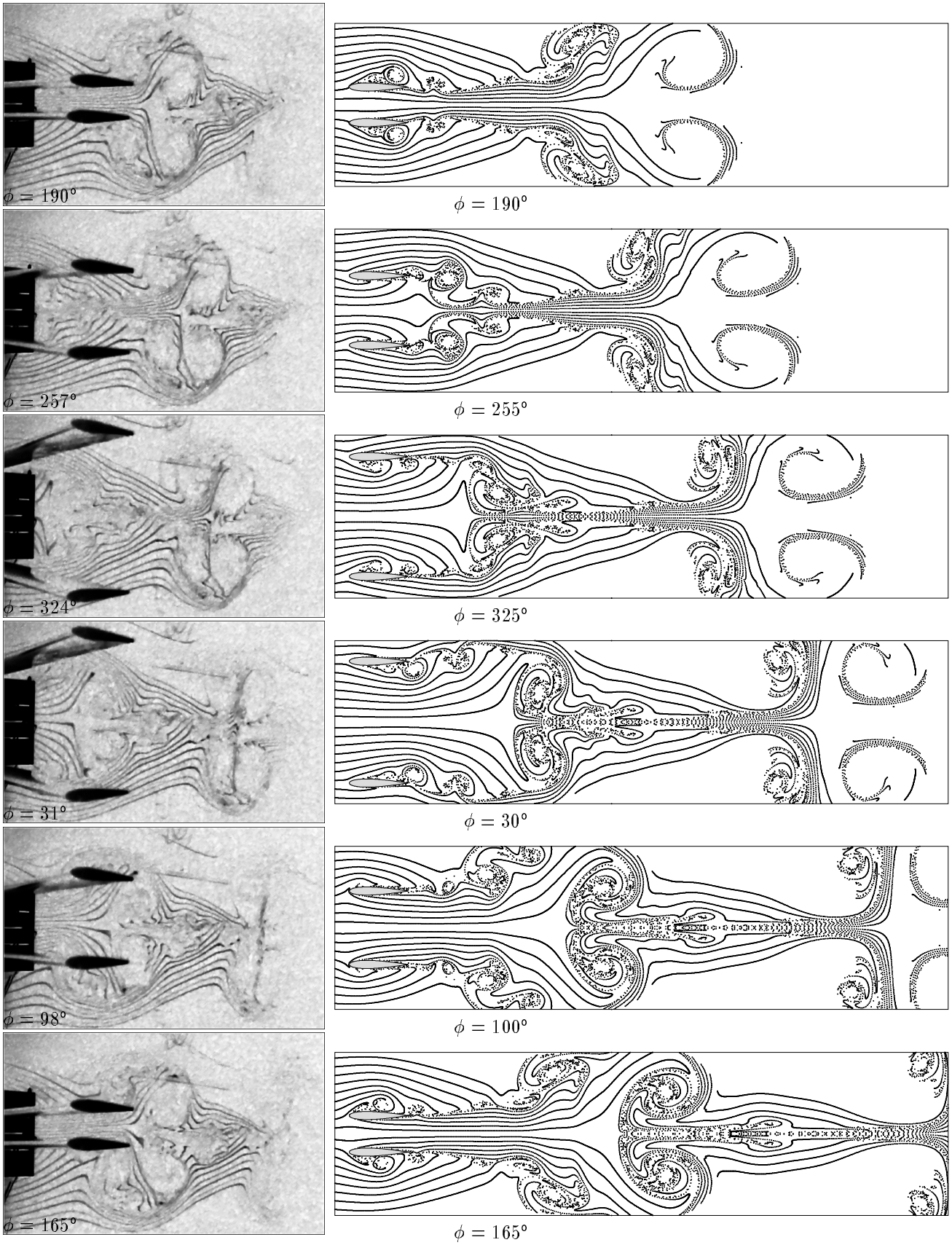

Fig. 21: Experimental and numerical streaklines, Re=10,000, k=1.

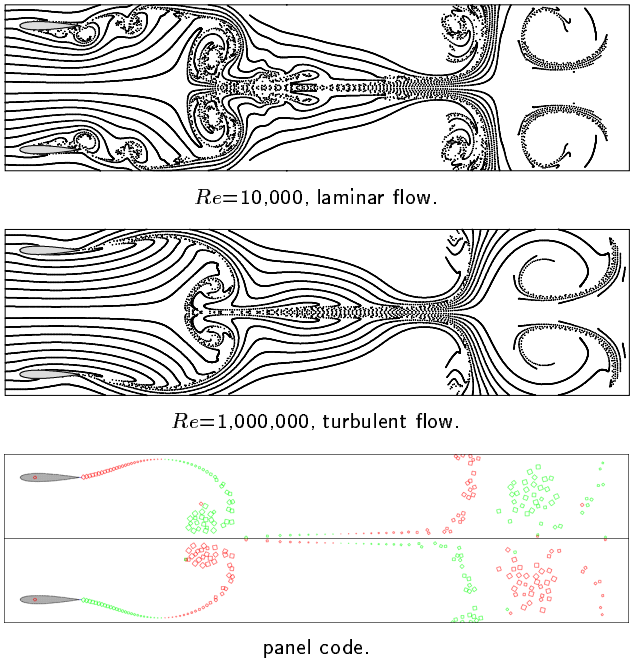

Fig. 22: Streaklines for k=1, ϕ=30 degrees.

Consequently, a more detailed experimental and numerical investigation was undertaken to further examine these issues both qualitatively and quantitatively.

In addition to the earlier measurements of thrust, detailed flow-visualization and wake velocity measurements were made to document the unsteady wake structures and velocity fields. Streaklines were produced using a smoke wire, and they were recorded on digital video. Unsteady frequency measurements were made using a synchronized strobe light. Unsteady velocity measurements were made using an LDV system coupled with a rotary motion resolver.

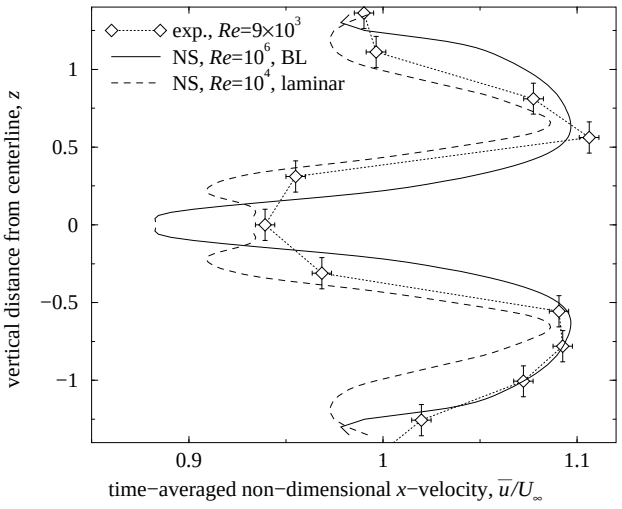

Fig. 23: Time-averaged wake profile for k=1.

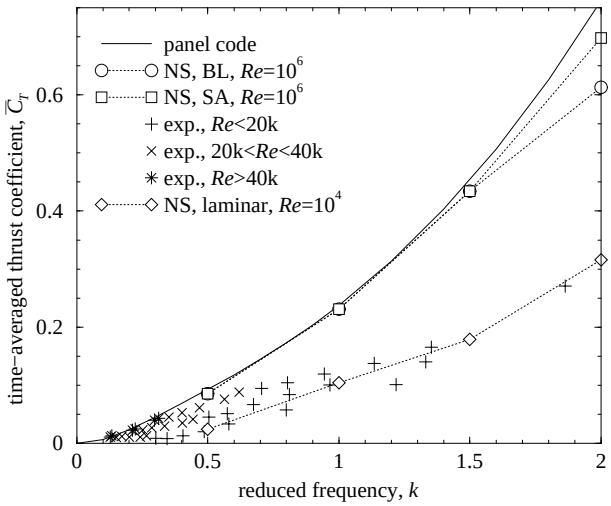

Fig. 24: Thrust coefficient versus k.

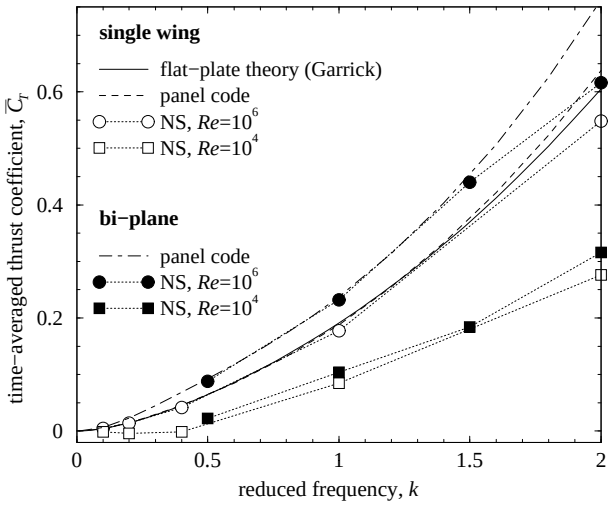

Fig. 25: Thrust coefficient versus k.

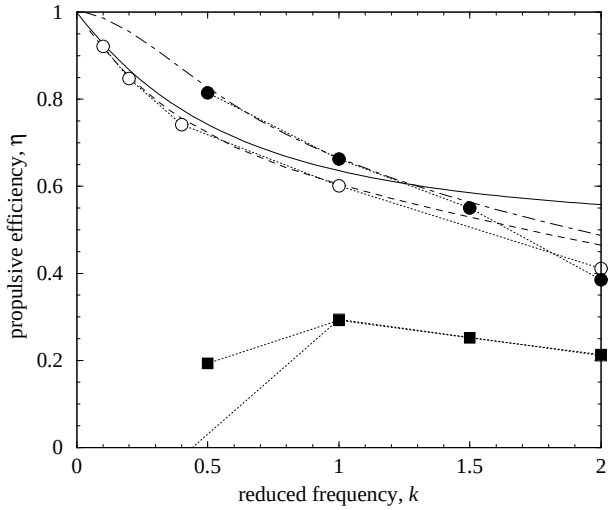

Fig. 26: Propulsive efficiency versus k.

An unsteady, compressible Navier-Stokes solver was modified to simulate the symmetric problem, utilizing a multi-block, deforming grid system, and operating on a parallel computer architecture. Additionally, particle-trace and time-averaged velocity data capabilities were added to the code to enable direct comparisons with the new experimental data. Unsteady simulations were run at $Re = 10^6$, assuming a fully turbulent boundary layer, and at $Re = 10^4$, assuming fully laminar flow.

The high-Re Navier-Stokes solutions agree well with the inviscid panel code results, and form an upper limit for the experimentally measured thrust, while the low-Re Navier-Stokes solutions form a lower limit for the experimental results. The wake structures predicted by the panel code agree well with the high-Re simulations, but both are quite different from the low-Re Navier-Stokes simulations, which bare a much better resemblance to the experimentally visualized wakes. Thrust data demonstrate that even at Reynolds numbers as low as 4×10^4 the inviscid panel code is a pretty good model, and wake-interference provides a substantial benefit. However, at a Reynolds number of 10^4, the panel code is no longer accurate, and the Navier-Stokes solver is needed. Additionally, at $Re = 10^4$, the benefits of wake-interference seem to be almost entirely lost.

Acknowledgments

This work was supported by the Naval Research Laboratory under project monitors Kevin Ailinger, Jill Dahlburg and Jim Kellogg, and through the Naval Postgraduate School's direct research program.

References

[1] Knoller, R., "Die Gesetze des Luftwiderstandes," **Flug- und Motortechnik (Wien)**, Vol. 3, No. 21, 1909, pp. 1-7.

[2] Betz, A., "Ein Beitrag zur Erklärung des Segelfluges," **Zeitschrift für Flugtechnik und Motorluftschiffahrt**, Vol. 3, Jan. 1912, pp. 269-272.

[3] Birnbaum, W., "Der Schlagflügelpropeller und die kleinen Schwingungen elastisch befestigter Tragflügel," **Zeitschrift für Flugtechnik und Motorluftschiffahrt**, Vol. 15, 1924, pp. 128-134.

[4] Katzmayr, R., "Effect of Periodic Changes of Angle of Attack on Behavior of Airfoils," NACA Report No. 147, Oct., 1922. (translated from **Zeitschrift für Flugtechnik und Motorluftschiffahrt**, Mar. 31, pp. 80-82, and Apr. 13, 1922, pp. 95-101).

[5] Garrick, I. E., "Propulsion of a Flapping and Oscillating Airfoil," NACA Report 567, 1936.

[6] Schmidt, W., "Der Wellpropeller, ein neuer Antrieb fuer Wasser-, Land-, und Luftfahrzeuge," Z. Flugwiss. Vol. 13, 1965, pp. 472-479.

[7] Jones, K. D. and Platzer, M. F., "Numerical Computation of Flapping-Wing Propulsion and Power Extraction," AIAA Paper No. 97-0826, Jan. 1997.

[8] Jones, K. D. and Platzer, M. F., "An Experimental and Numerical Investigation of Flapping-Wing Propulsion," AIAA Paper No. 99-0995, Jan. 1999.

[9] Lund, T. C., "A Computational and Experimental Investigation of Flapping Wing Propulsion," Master's Thesis, Dept. of Aeronautics and Astronautics, Naval Postgraduate School, Monterey, CA, March 2000.

[10] Jones, K. D. and Platzer, M. F., "Flapping-Wing Propulsion for a Micro Air Vehicle," AIAA Paper No. 2000-0897, Jan. 2000.

[11] Jones, K. D., Duggan, S. J. and Platzer, M. F., "Flapping-Wing Propulsion for a Micro Air Vehicle," AIAA Paper No. 2001-0126, Jan. 2001.

[12] Teng, N. H., "The Development of a Computer Code for the Numerical Solution of Unsteady, Inviscid and Incompressible Flow over an Airfoil," Master's Thesis, Naval Postgraduate School, Monterey, CA, June 1987.

[13] Jones, K. D. and Center, K. B., "Numerical Wake Visualization for Airfoils Undergoing Forced and Aeroelastic Motions," AIAA Paper No. 96-0055, Jan. 1996.

[14] Hess, J. L. and Smith, A. M. O., "Calculation of Potential Flow about Arbitrary Bodies," **Progress in Aeronautical Sciences**, Vol. 8, pp. 1-138, Pergamon Press, Oxford, 1966.

[15] Basu, B. C. and Hancock, G. J., "The Unsteady Motion of a Two-Dimensional Aerofoil in Incompressible Inviscid Flow," **Journal of Fluid Mechanics**, Vol. 87, 1978, pp. 159-168.

[16] Platzer, M. F., Neace, K. S. and Pang, C. K., "Aerodynamic Analysis of Flapping Wing Propulsion," AIAA Paper No. 93-0484, Jan. 1993.

[17] Jones, K. D., Dohring, C. M. and Platzer, M. F., "Experimental and Computational Investigation of the Knoller-Betz Effect," **AIAA Journal**, Vol. 36, No. 7, July 1998.

[18] Jones, K. D., Lund, T. C. and Platzer, M. F., "Experimental and Computational Investigation of Flapping Wing Propulsion for Micro-Air Vehicles," Chapter 16, AIAA Progress in Astronautics and Aeronautics, Vol. 195, Fixed and Flapping Wing Aerodynamics for Micro Air Vehicle Applications, Ed. T. Mueller, AIAA, Reston, VA, 2001, pp. 307-339.

[19] Castro, B. M., "Multi-Block Parallel Navier-Stokes Simulation of Unsteady Wind Tunnel and Ground Interference Effects," Ph.D. Thesis, Dept. of Aeronautics and Astronautics, Naval Postgraduate School, Monterey, CA, Sept. 2001.

[20] Ekaterinaris, J. A. and Menter, F. R., "Computation of Oscillating Airfoil Flows with One- and Two-Equation Turbulence Models," **AIAA Journal**, Vol. 32, No. 12, 1994, pp. 2359-2365.

[21] Thomas, P. D. and Lombard, C. K., "Geometric Conservation Law and its Applications to Flow Computations on Moving Grids," **AIAA Journal**, Vol. 17, No. 10, 1979, pp. 1030-1037.

[22] Osher, S. and Chakravarthy, S. R., "A New Class of High Accuracy TVD Schemes for Hyperbolic Conservation Laws," AIAA Paper No. 85-0363, 1985.

[23] Chakravarthy, S. R. and Osher, S., "Numerical Experiments with the Osher Upwind Scheme for the Euler Equations," **AIAA Journal**, Vol. 21, No. 11, 1983, pp. 1241-1248.

[24] Steger, J. L. and Warming, R. F., "Flux Vector Splitting of the Inviscid Gas Dynamic Equations with Applications to Finite-Difference Methods," **Journal of Computational Physics**, Vol. 40, 1981, pp. 263-293.

[25] Baldwin, B. S. and Lomax, H., "Thin Layer Approximation and Algebraic Model for Separated Turbulent Flow," AIAA Paper No. 78-257, 1978.

[26] Baldwin, B. S. and Barth, T. J., "A One-Equation Turbulence Transport Model for High Reynolds Number Wall-Bounded Flows," NASA TM 102847, 1990.

[27] Spalart, P. R. and Allmaras, S. R., "A One-Equation Turbulence Model for Aerodynamic Flows," AIAA Paper No. 92-0439, 1992.

[28] Mahmoud, O. M. K. M., "Experimental Investigation of Low Speed Flow Over Flapping Airfoils and Airfoil Combinations," Ph.D. Thesis, Dept. of Aeronautics and Astronautics, Naval Postgraduate School, Monterey, CA, Sept. 2001.